Matter, Volume *5*

Supplemental information

A sustainable chitosan-zinc electrolyte for high-rate zinc-metal batteries

Meiling Wu, Ye Zhang, Lin Xu, Chunpeng Yang, Min Hong, Mingjin Cui, Bryson C. Clifford, Shuaiming He, Shuangshuang Jing, Yan Yao, and Liangbing Hu

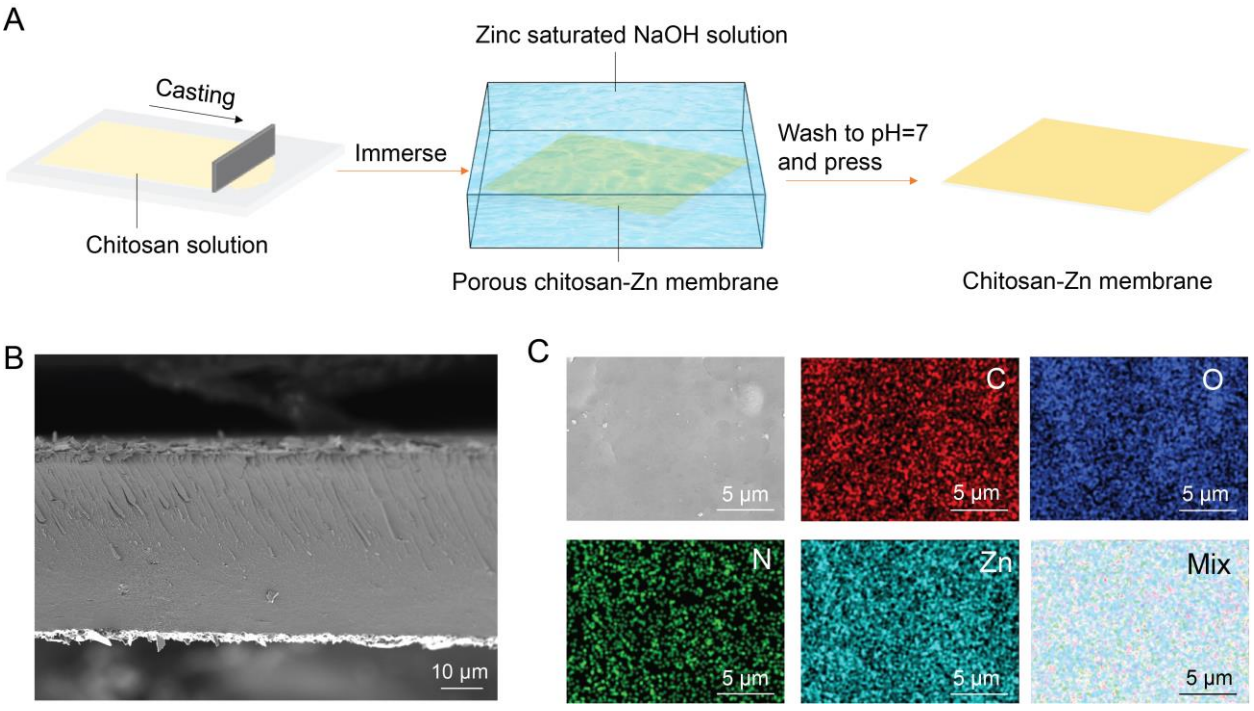

Figure S1. Fabrication and characterizations of the chitosan-Zn membrane. (A) Schematic diagram of the preparation of the chitosan-Zn membrane. Chitosan solution is first cast on a PET support (left), then immediately immerse in a Zn^{2+}-saturated NaOH solution (middle). The resulting porous chitosan-Zn membrane is rinsed with water and mechanically pressed to obtain the final densified chitosan-Zn membrane (right). (B) A cross-sectional SEM image revealing the densified structure. (C) EDS elemental mapping of C, O, N and Zn in the densified chitosan-Zn membrane indicates the elements are uniformly distributed.

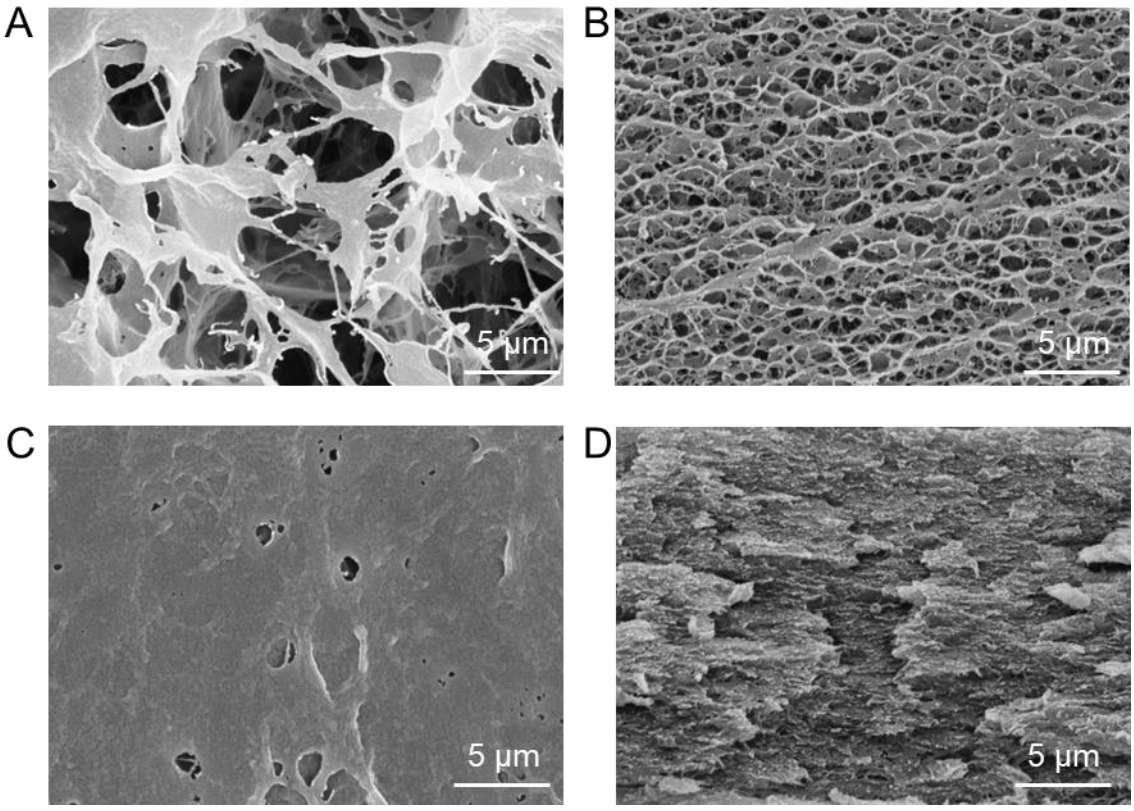

Figure S2. Morphology of the porous and densified chitosan membranes. (A) The surface and (B) cross-sectional morphology of the porous chitosan membrane. (C) The surface and (D) cross-sectional morphology of the chitosan membrane after pressing. The porous chitosan membrane displays a hierarchical porous structure, which is similar to the porous chitosan-Zn membrane. After densification, the pores are eliminated, resulting in a dense structure.

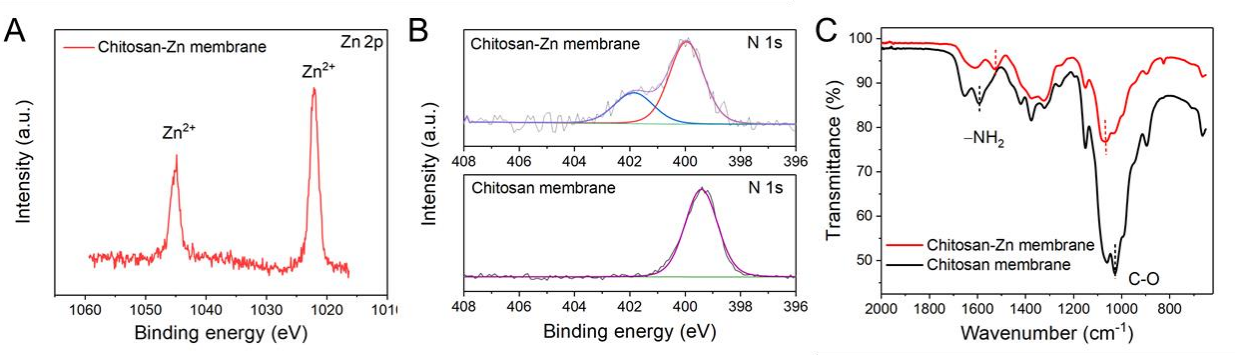

Figure S3. XPS and FTIR analysis of the densified chitosan-Zn and chitosan membranes. (A) The Zn 2p XPS spectrum of the chitosan-Zn membrane. (B) The XPS N1s spectra of the chitosan-Zn and chitosan membranes. C) The FTIR spectra of the chitosan-Zn and chitosan membranes.

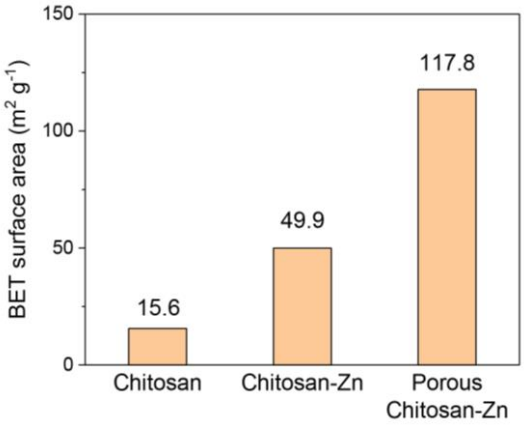

Figure S4. Comparison of BET surface area. The BET surface area of the densified chitosan, densified chitosan-Zn, and porous chitosan-Zn membranes.

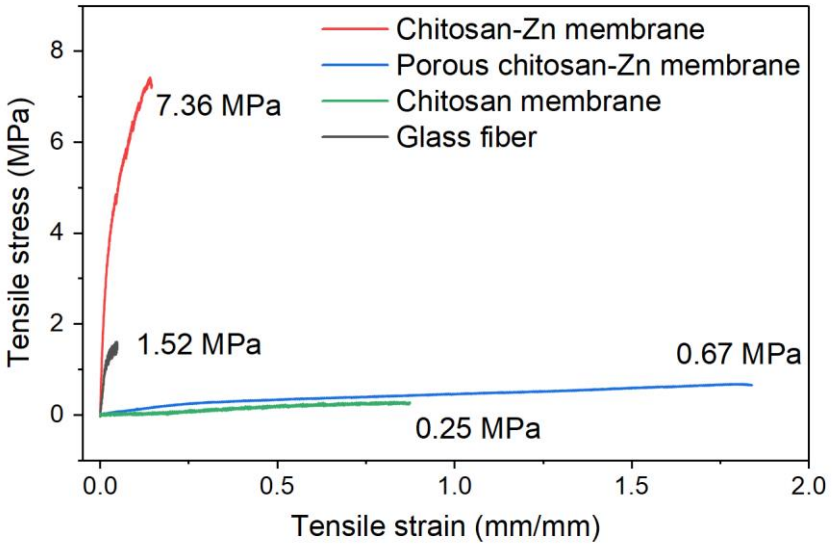

Figure S5. Mechanical strength comparison. The tensile stress-strain curves of the wet densified chitosan-Zn (mimicking the battery conditions), wet porous chitosan-Zn, densified chitosan, and a glass fiber membrane. The densified chitosan-Zn membrane shows a much higher strength than the glass fiber separator that is commonly used in Zn-metal batteries. In addition, the higher tensile stress of the chitosan-Zn membrane (7.36 MPa) compared to the porous chitosan-Zn (0.67 MPa) and chitosan membranes (0.25 MPa) indicates that both Zn^{2+} coordination and the densification process increases the material's mechanical strength.

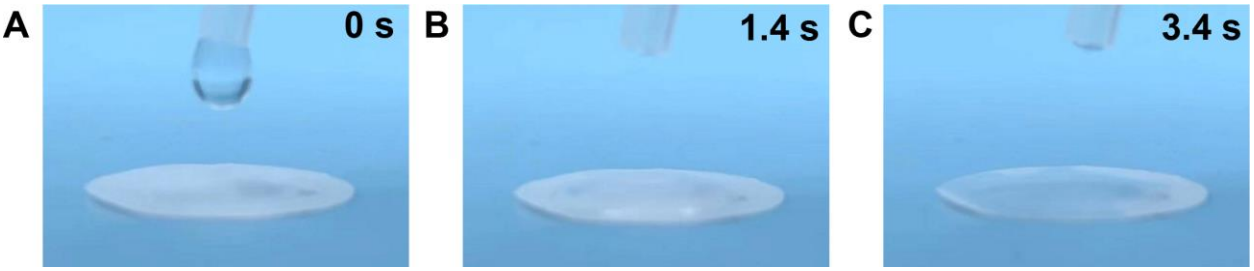

Figure S6. Snapshot photos of 2 M $ZnSO_4$ aqueous solution wetting ability on densified chitosan-Zn electrolyte: (A) 0 s; (B) 1.4 s; and (C) 3.4 s. The pristine chitosan-Zn membrane is semitransparent (Figure S6a). After adding a drop of $ZnSO_4$ aqueous solution on it, aqueous solution spreads to the whole surface of chitosan-Zn membrane quickly (Figure S6b), indicating a strong hydrophilic property. After 2 s, a transparent color in chitosan-Zn membrane is observed (Figure S6c), suggesting the aqueous solution penetrates the chitosan-Zn membrane, which also demonstrates that the aqueous solution has an excellent wetting ability to the chitosan-Zn membrane.

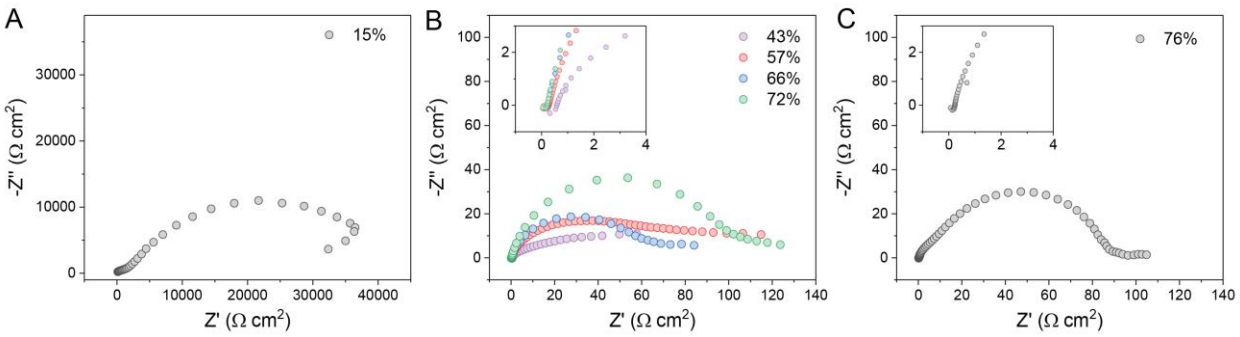

Figure S7. EIS of the chitosan-Zn electrolytes and pure aqueous electrolyte. EIS curves of the chitosan-Zn electrolytes with different water contents, including (A) 15% and (B) 43–72%, as well as the (C) 2 M $ZnSO_4$ aqueous electrolyte (76% water content). Zn||Zn cells are applied to measure the conductivity of the chitosan-Zn/$ZnSO_4$ electrolyte. The intercept at the x-axis (high frequency region) indicates the resistance of the electrolyte, which was used to calculate the ionic conductivities of the different samples.

A

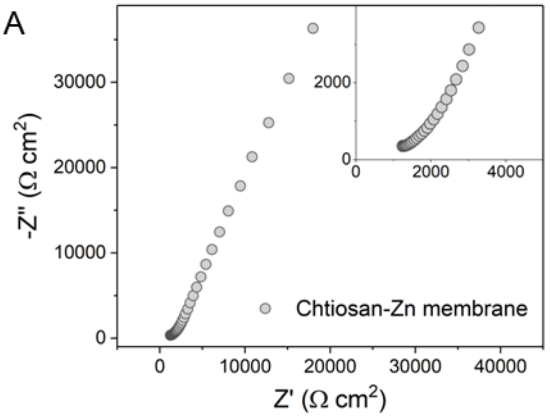

B

Material	σ (S cm^{-1})
Chitosan-Zn/$ZnSO_4$ electrolyte	7.18×10^{-2}
Chitosan-Zn membrane without $ZnSO_4$	1.22×10^{-5}

Figure S8. Comparison of Zn^{2+} conductivity. (A) EIS curve of the densified chitosan-Zn membrane. The chitosan-Zn membrane is fabricated with a similar process with that of chitosan-Zn electrolyte, except that the 2 M $ZnSO_4$ immersing process is not applied. (B) Comparison of Zn^{2+} conductivity between densified chitosan-Zn electrolyte and chitosan-Zn membrane without $ZnSO_4$.

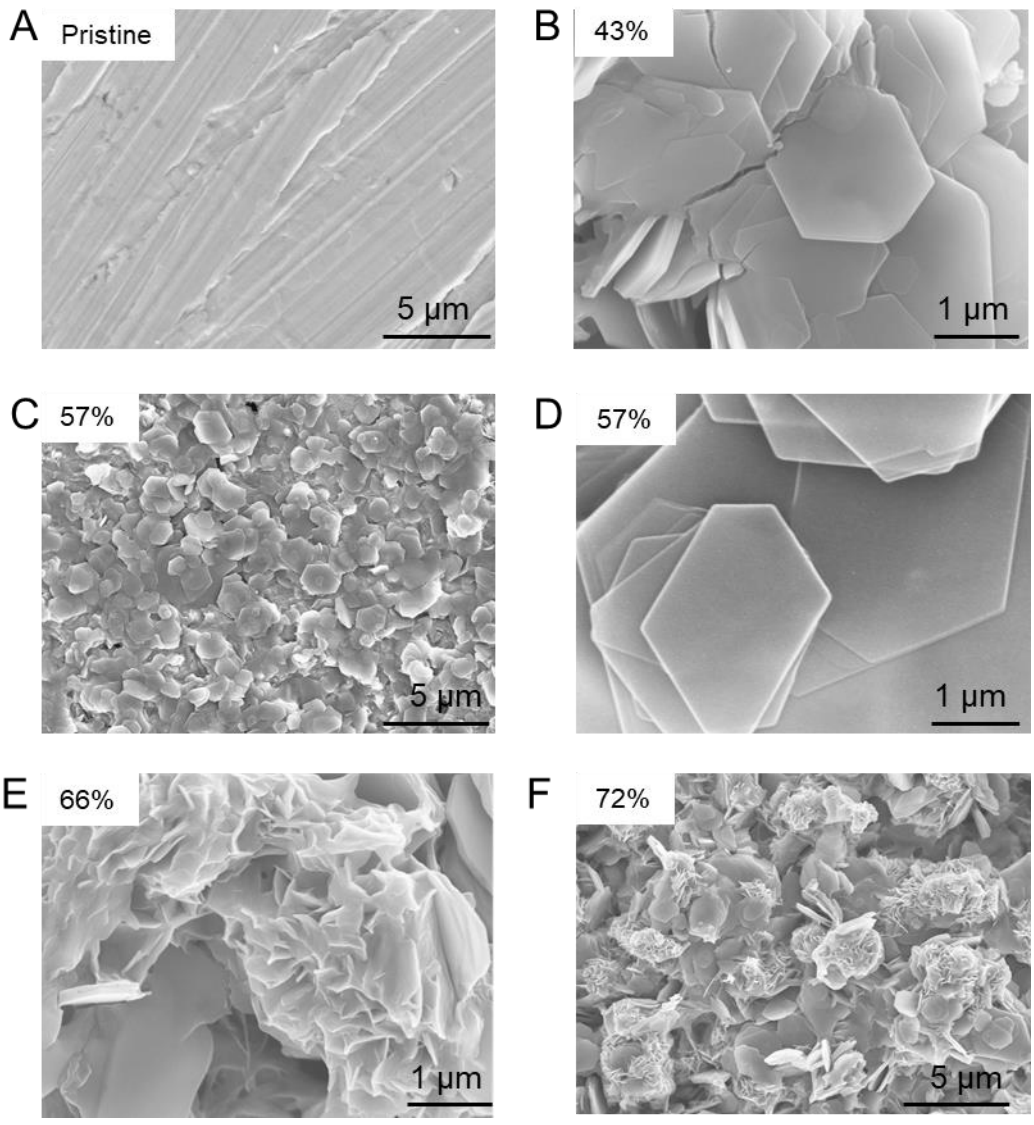

Figure S9. Zn plating morphology. (A) The surface morphology of the pristine Zn metal, used as the electrodes in the Zn||Zn cells. (B–F) The surface morphology of the Zn anode in Zn||Zn cells after plating at 20 mA cm^{-2} and 4 mAh cm^{-2} for 50 cycles using chitosan-Zn electrolytes with different water contents of (B) 43%, (C, D) 57%, (E) 66%, and (F) 72%. When applying chitosan-Zn electrolytes with water contents of 43% and 57%, the electrochemically deposited Zn displays hexagonal platelets stacked parallel on the Zn electrode surface, which is beneficial for reducing the interfacial area between the Zn anode and electrolyte, and thus the interfacial resistance. With increased water content

(e.g., 66% and 72%), the plated Zn is moss-like in morphology, with a large surface area and the potential to form dead Zn and even short circuits induced by dendritic penetration through the electrolyte.

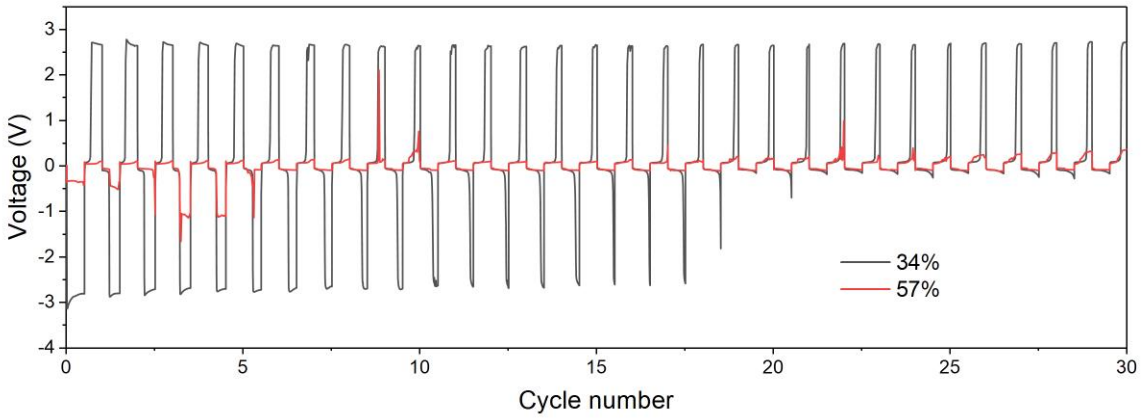

Figure S10. Voltage profiles of the galvanostatic Zn plating/stripping of the chitosan-Zn electrolytes. (a) The voltage profiles of Zn||Zn cells cycled at 20 mA cm^{-2} and 4 mAh cm^{-2} using chitosan-Zn electrolytes with 34% and 57% water contents. The cell using chitosan-Zn electrolyte with 34% water content shows a higher plating overpotential than that of 57% water content.

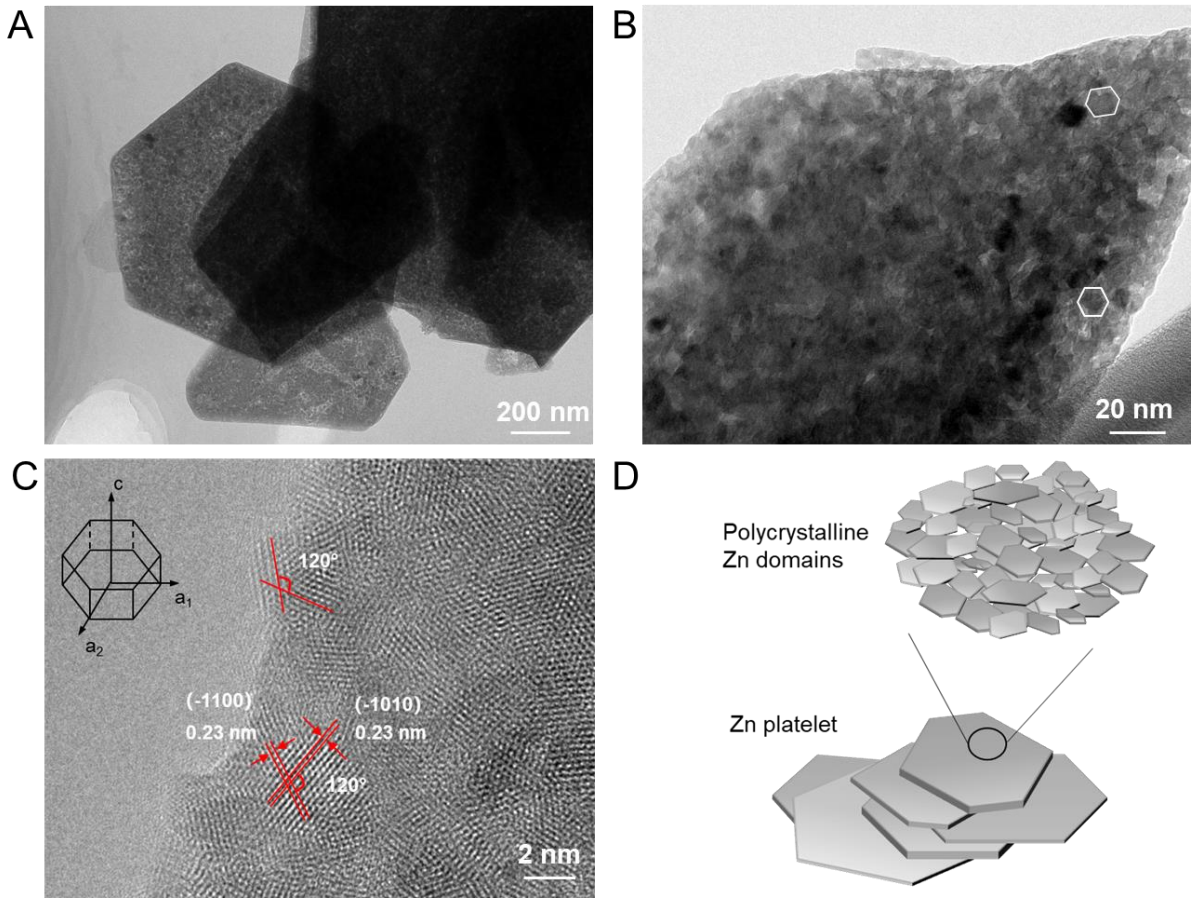

Figure S11. TEM measurements of the Zn plating morphology. (A) TEM image of Zn platelets with hexagonal shape formed on the anode of Zn||Zn cells using chitosan-Zn electrolyte with 57% water content. (B) Magnified TEM image of a Zn platelet. (C) A high-resolution TEM image of a Zn platelet and schematic diagram of the Zn unit cell in the inset. The lattice distance (0.23 nm) is consistent with the distance between (−1010) planes. In addition, the angle between the (−1100) and (−1010) plane is 120°. (D) Schematic diagram of the Zn platelets composed of small polycrystalline Zn platelets. The Zn platelets in a–c were obtained after plating at 20 mA cm^{-2} and 4 mAh cm^{-2} for 50 cycles.

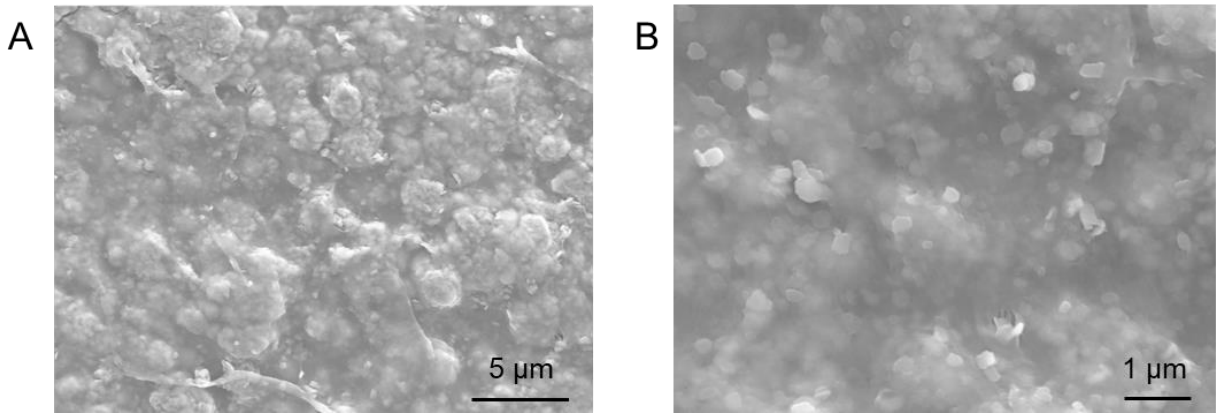

Figure S12. Zn plating morphology. The Zn anode surface morphology in Zn||Zn cells using chitosan-Zn electrolyte with 57% water content after plating at 10 mA cm^{-2} and 2 mAh cm^{-2} for 20 cycles: (A) Low magnification; (B) High magnification. Small Zn platelets with a size of ~200 nm begin to appear, demonstrating a hexagonal shape.

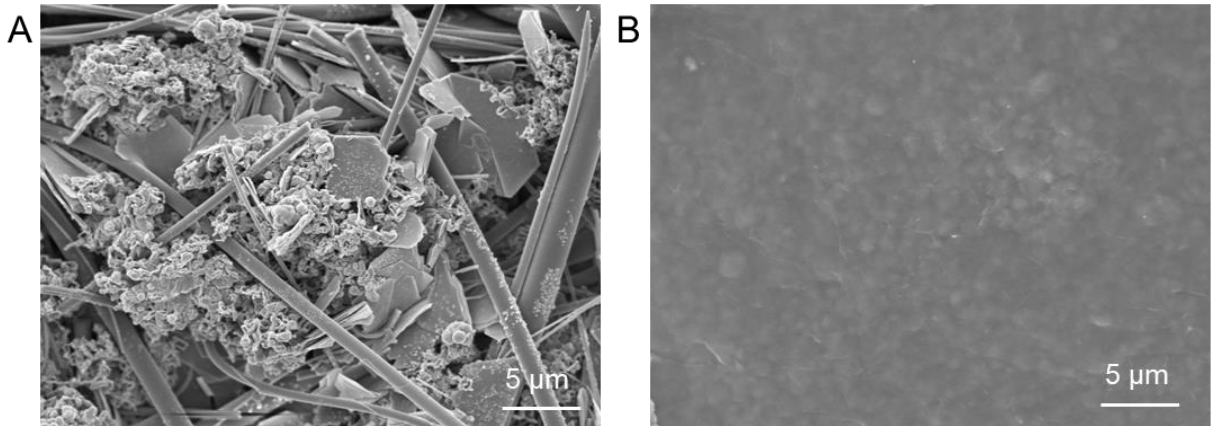

Figure S13. Morphology of the aqueous electrolyte with glass fiber and chitosan-Zn electrolyte after Zn plating/stripping. The electrolyte surface morphology in Zn||Zn cells after plating at 10 mA cm^{-2} and 2 mAh cm^{-2} for 50 cycles using different electrolytes: (A) the aqueous electrolyte with a glass fiber as a separator; and (B) chitosan-Zn electrolyte with 57% water content. To observe the morphology of both electrolytes by SEM, both samples are freeze-dried to remove the water inside the membranes. The fibers, platelets, and particle aggregation in (a) are ascribed to the glass fibers, randomly orientated Zn platelets, and $ZnSO_4$, respectively. The randomly orientated Zn platelets are able to penetrate the glass fiber separator, reducing the cell lifetime. Meanwhile, the chitosan-Zn electrolyte maintains a dense, uniform surface.

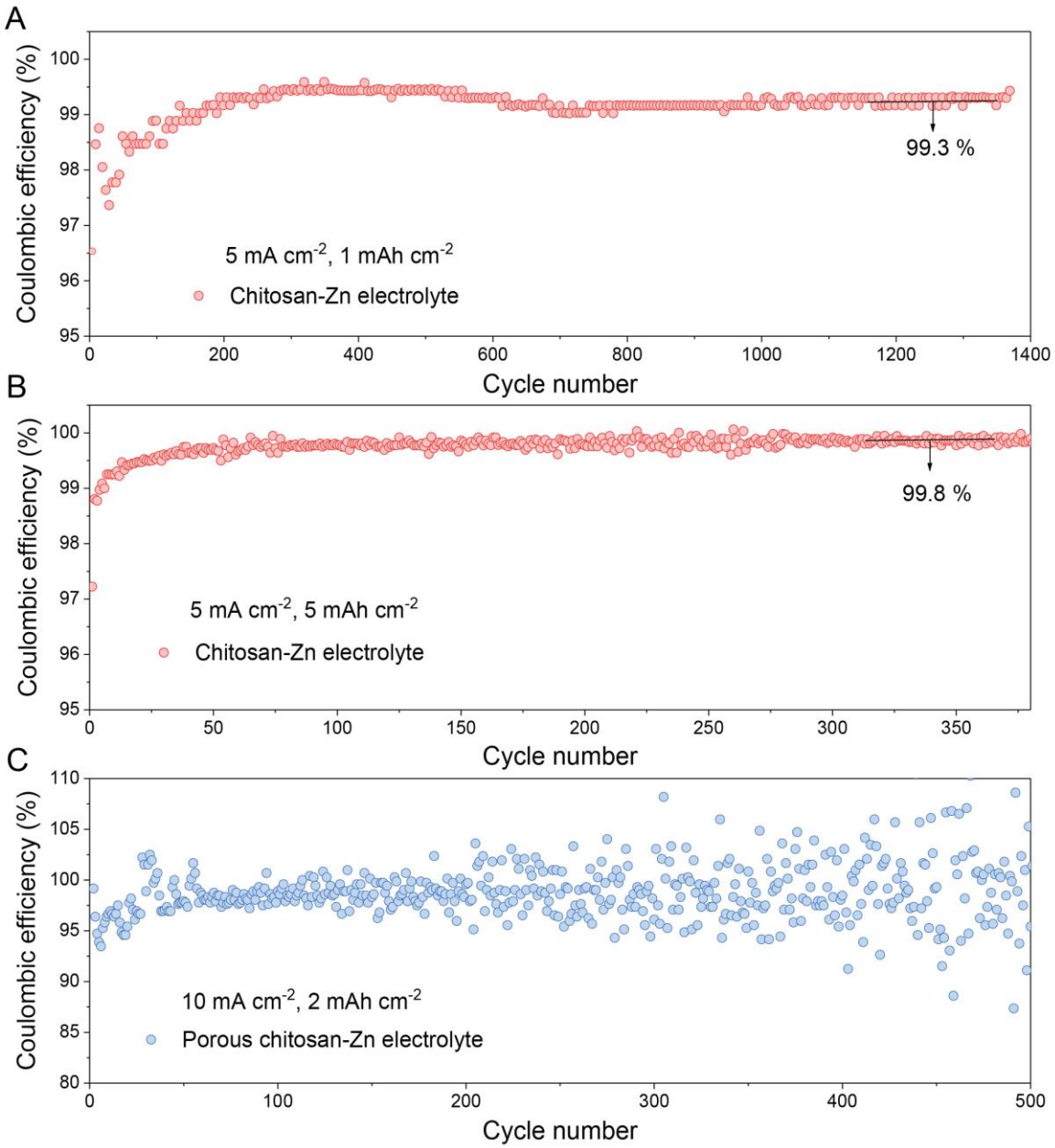

Figure S14. Coulombic efficiency of the Zn||Cu cell using the (A and B) chitosan-Zn electrolyte and (C) porous chitosan-Zn electrolyte (i.e., without densifying). The Zn plating/striping Coulombic efficiency on a Cu electrode cycled with chitosan-Zn electrolyte at (A) 5 mA cm^{-2} and 1 mAh cm^{-2}; and (B) 5 mA cm^{-2} and 5 mAh cm^{-2}. (C) The Zn plating/striping Coulombic efficiency on a Cu electrode cycled with the porous chitosan-Zn electrolyte at 10 mA cm^{-2} and 2 mAh cm^{-2}.

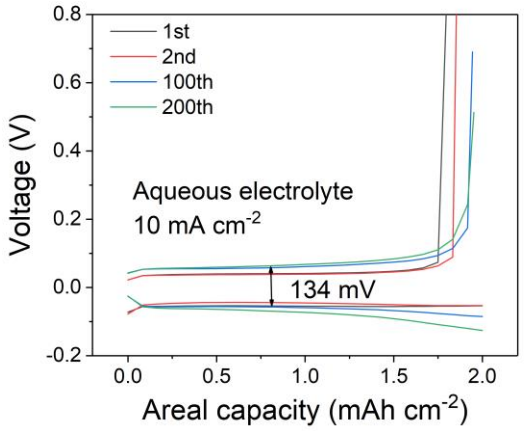

Figure S15. The Zn plating/striping voltage profiles of the Zn||Cu cell using aqueous electrolyte. Zn plating/striping on a Cu electrode cycled with aqueous electrolyte at 10 mA cm^{-2} and 2 mAh cm^{-2}.

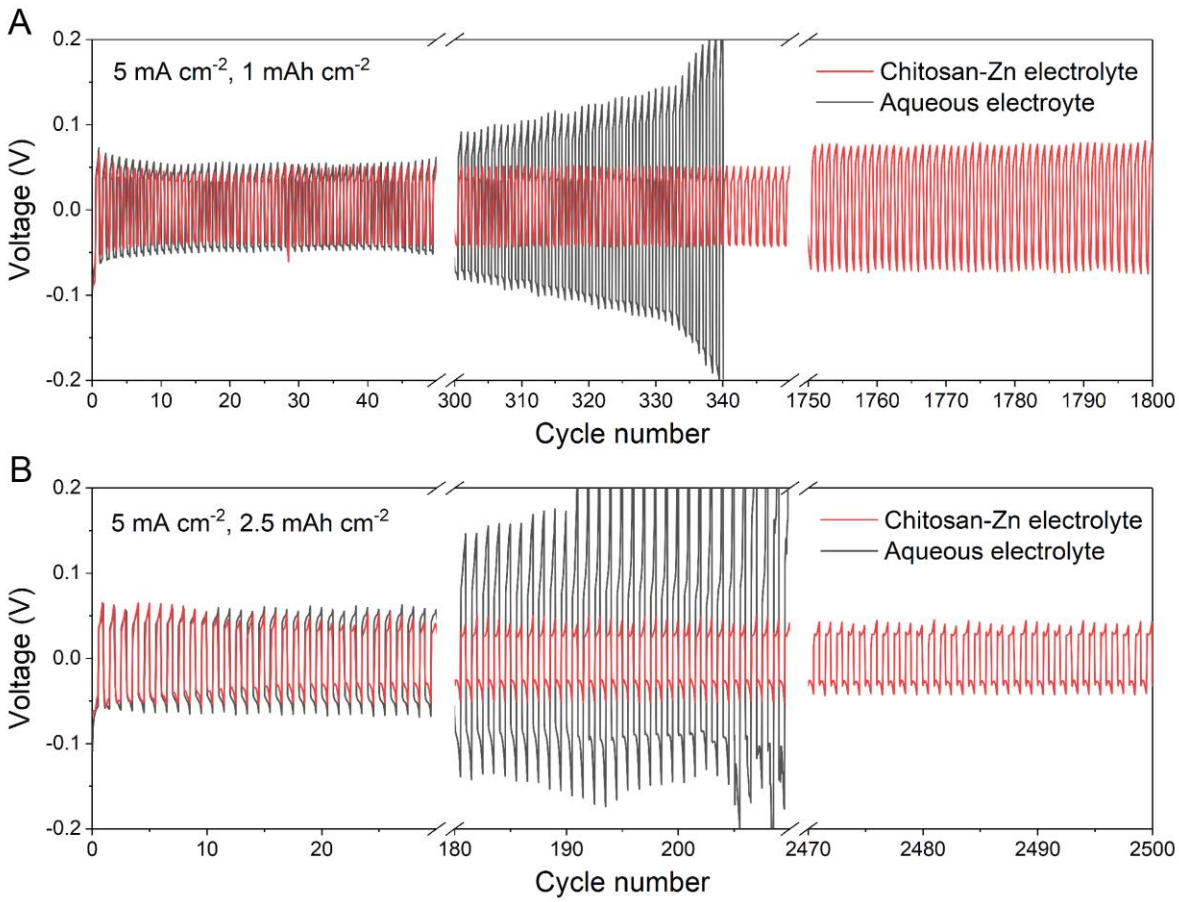

Figure S16. Galvanostatic Zn plating/striping. Galvanostatic Zn plating/striping in a Zn||Zn cell using chitosan-Zn electrolyte and aqueous electrolyte at (A) 5 mA cm^{-2} and 1 mAh cm^{-2}, and (B) 5 mA cm^{-2} and 2.5 mAh cm^{-2}.

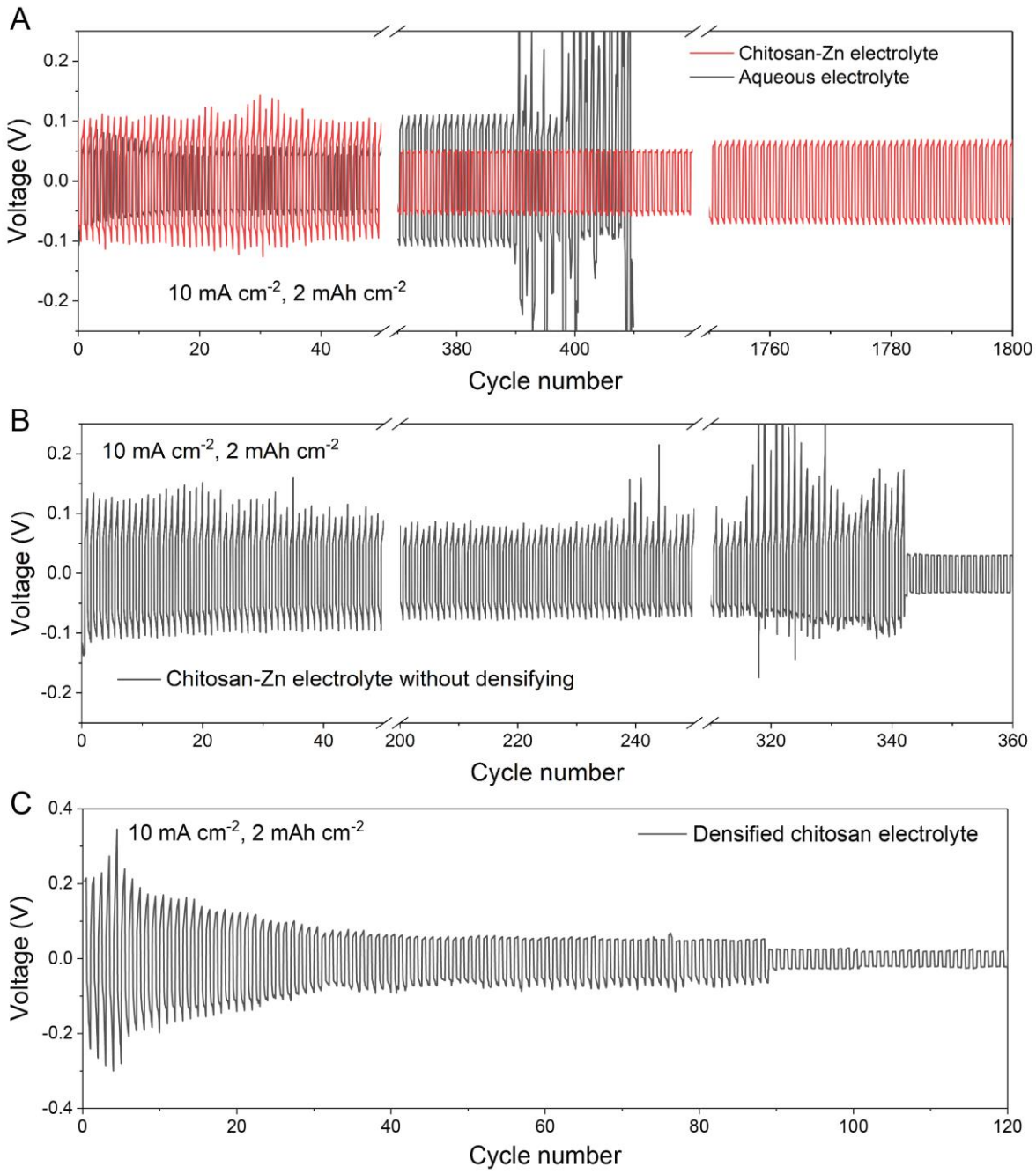

Figure S17. Galvanostatic Zn plating/striping. Galvanostatic Zn plating/striping in a Zn||Zn symmetric cell using the (A) porous chitosan-Zn electrolyte and aqueous electrolyte, (B) chitosan-Zn electrolyte without densifying, and (C) densified chitosan electrolyte (without Zn^{2+} coordination) at 10 mA cm^{-2} and 2 mAh cm^{-2}.

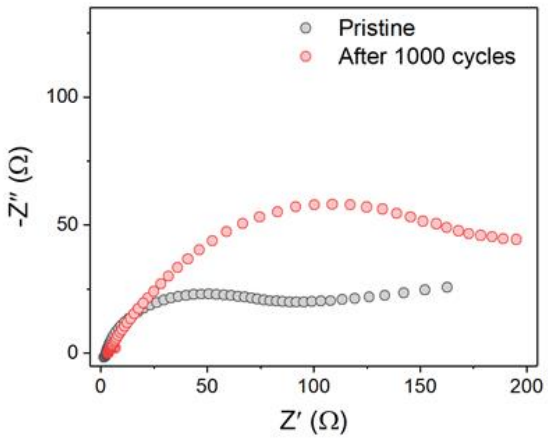

Figure S18. EIS spectra of the Zn||Zn symmetric cell: Pristine Zn||Zn cell (Black dots) and Zn||Zn cell after cycling at 10 mA cm^{-2} and 2 mAh cm^{-2} for 1000 cycles (Red dots).

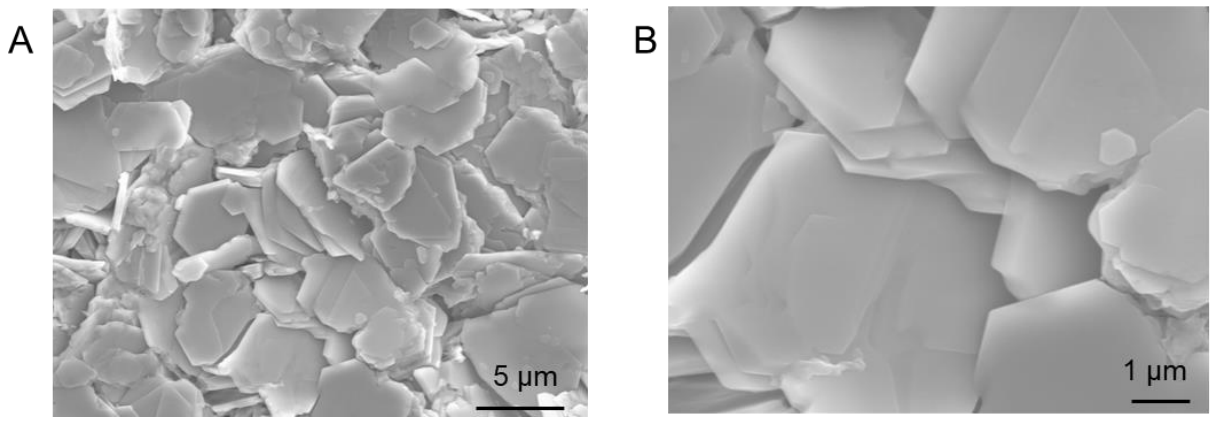

Figure S19. Zn anode surface morphology after galvanostatic Zn plating/striping: (A) Low magnification; (A) High magnification. The Zn anode surface morphology in Zn||Zn cells after plating at 10 mA cm^{-2} and 2 mAh cm^{-2} for 1000 cycles using the chitosan-Zn electrolyte. The hexagonal Zn platelets are maintained.

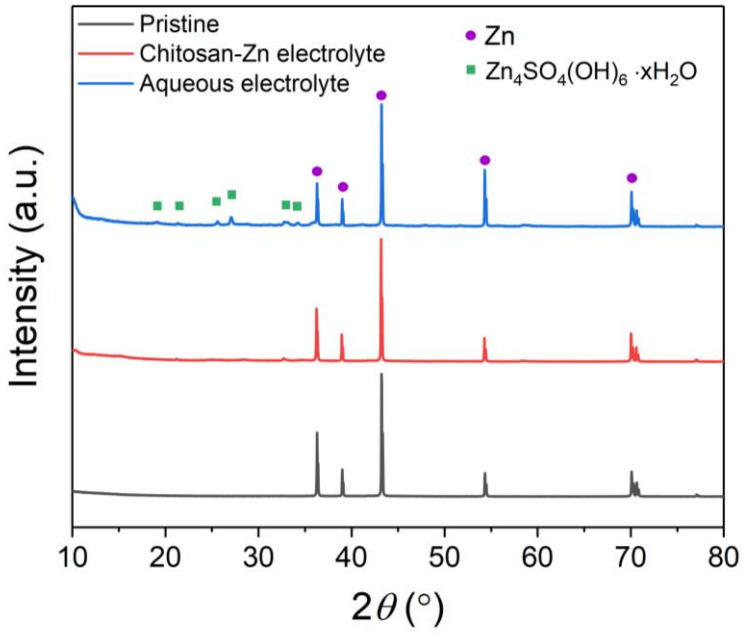

Figure S20. XRD measurements of the Zn anode. XRD patterns of pristine Zn and the Zn anode in Zn||Zn cells after plating/stripping at 10 mA cm^{-2} and 2 mAh cm^{-2} for 400 cycles using chitosan-Zn and aqueous electrolytes. There are obvious peaks (indicated by green squares) in the XRD curve of the Zn anode using the aqueous electrolyte, which are ascribed to the side product of $Zn_4SO_4(OH)_6 \cdot xH_2O$ [1]. This product is present but less detectable in the XRD curve of the Zn anode using the chitosan-Zn electrolyte, suggesting chitosan-Zn electrolyte can suppress the production of side product efficiently. The peaks indicated by the purple dots are ascribed to plating Zn and substrate Zn.

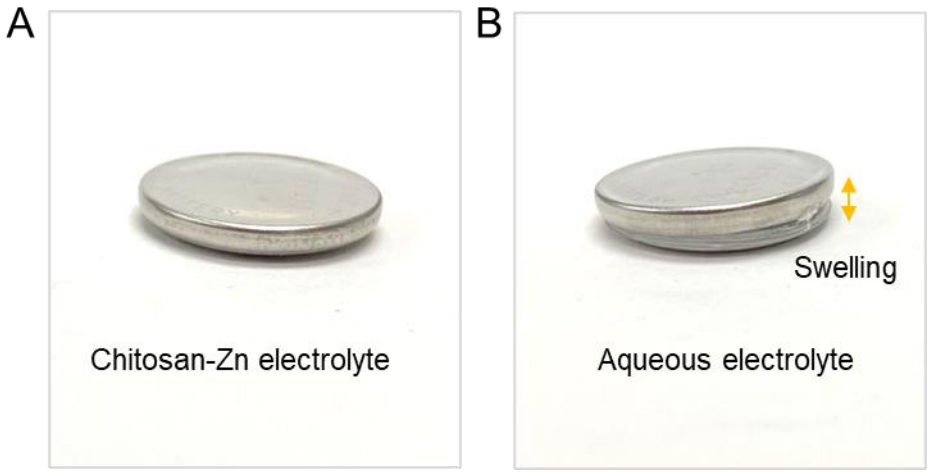

Figure S21. Comparison of swelling in coin cells after Zn plating using the chitosan-Zn and aqueous electrolytes. Digital photos of Zn||Zn coin cells after plating at 50 mA cm^{-2} and 10 mAh cm^{-2} for 100 cycles using (A) chitosan-Zn and (B) aqueous electrolytes. The coin cell using the aqueous electrolyte swells to rupture due to the cumulative H_2 gas evolved from H_2 evolution reaction from the excess water in the aqueous electrolyte during the Zn plating process. Meanwhile, the coin cell using the chitosan-Zn electrolyte remained intact and no obvious swelling is observed, indicating the ability of the chitosan-Zn electrolyte to suppress the H_2 evolution due to limited free water in chitosan-Zn electrolyte.

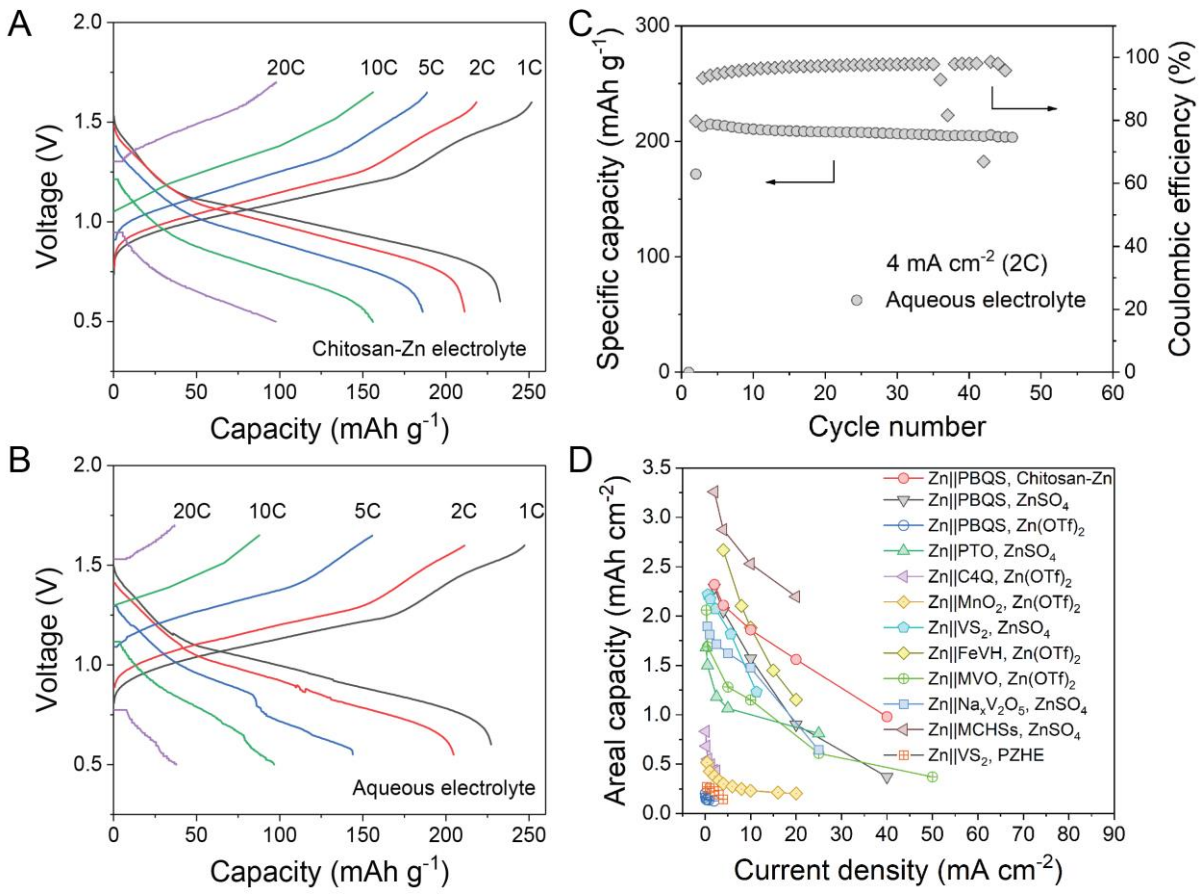

Figure S22. Performance of the Zn-metal full cell. Galvanostatic charge-discharge potential profiles of the Zn||PBQS cell at different rates using (A) chitosan-Zn electrolyte and (B) aqueous electrolyte. (C) The cycling performance of the Zn||PBQS cell in 2 M $ZnSO_4$ at 2C with a PBQS loading of 10 mg cm^{-2}. (D) Performance comparison of Zn-metal batteries with different electrolytes [2-12] in terms of the current density and areal capacity.

Table S1. Ionic conductivity comparison of reported Zn^{2+} electrolytes.

No	Material	Conductivity (mS cm^{-1})	Ref.
1	Chitosan-Zn electrolyte	71.8	This work
2	Chitosan-biocellulosics	86.7	[13]
3	Cellulose-based hydrogel	7409	[14]
4	PVA/nanocellulose hydrogel	18.1	[15]
5	Gelatin-based solid-state electrolyte	16	[16]
6	Polyacrylamide hydrogel/2 M $ZnSO_4$+4 M LiCl/H_2O	25	[17]
7	$Zn(OTf)_2$/7 Triethyl phosphate : 3 H_2O	6.48	[18]
8	2 M $Zn(BF_4)_2$ / [EMIM]BF_4 ionic liquid	16.9	[19]
9	2 M $ZnSO_4$/H_2O+EG (50 vol % EG)	7.5	[20]
10	Water-in-deep eutectic solvent	1.85	[21]
11	2 M $ZnSO_4$/H_2O	53	[20]

Table S2. Performance comparison of galvanostatic Zn plating/striping between different electrolytes in Zn||Zn cells.

No	Anode	Material	Current density (mA cm^{-2})	Areal Capacity (mAh cm^{-2})	Cycles	Polarization voltage (mV)	Reference
1	Zn foil	Chitosan-Zn electrolyte	5	1	1800	50	This work
2	Zn foil	Chitosan-Zn electrolyte	10	2	1800	50	
3	Zn foil	Chitosan-Zn electrolyte	50	10	1000	374	
4	Zn foil	2 M $ZnSO_4$	50	10	350	370	
5	Zn foil	Polyacrylamide hydrogel/2 M $ZnSO_4$+4 M LiCl/H_2O	1	1	200	80	[17]
6	3D Zn	Chitosan-biocelllulosics	25	3.33	3000	<200	[13]
7	ZrO_2-coated Zn	2 M $ZnSO_4$	5	1	5250	32	[22]
8	Zn foil	$ZnCl_2$ 2.33 H_2O	5	1	2500	25	[23]
9	Zn foil	$ZnCl_2$ 2.33 H_2O	10	1	2400	75	[23]
10	Zn foil	$Zn(OTf)_2$/7 Triethyl phosphate : 3 H_2O	0.5	5	100	50	[18]
11	Zn foil	2 M $Zn(BF_4)_2$ / $[EMIM]BF_4$ ionic liquid	2	1	1500	75	[19]
12	Zn foil	1 m $Zn(TFSI)_2$+20 m LiTFSI/H_2O	0.2	0.035	500	150	[24]
13	Zn on carbon felt	2 M $ZnBr_2$+3 M KCl	40	20	290	~55	[25]
14	Zn foil	1 M $ZnSO_4$/H_2O+ AN (15 vol %)	2	2	300	~80	[14]
15	Zn foil	2 M $ZnSO_4$/H_2O+ EG (50 vol %)	1	1	600	50	[20]
16	Zn foil	Water-in-deep eutectic solvent	0.1	0.074	1622	100	[21]
17	Zn foil	3 M $Zn(OTf)_2$ + Et_2O (2 vol %)	0.2	0.2	125	30	[26]

Table S3. The fabrication cost of the chitosan-Zn electrolyte.

Chemicals	Price (USD/kg) [a]	Mass (kg)	Cost (USD/kg electrolyte)	$Cost_{all}$ (USD/kg electrolyte) [b]	$Cost_{all}$ (USD/m^2 electrolyte)
Chitosan	59	6	0.354	46.55	4.19
NaOH	0.33	100	0.033		
$ZnSO_4$	0.4	80	0.032		

[a] Prices are sourced from Alibaba.

[b] Chitosan-Zn electrolyte with a dry mass of 90 g and a size of 1 m^2 was produced from 60 g chitosan, 100 g NaOH, and 80 g $ZnSO_4$.

REFERENCES

1. Yang, Q., Li, Q., Liu, Z., Wang, D., Guo, Y., Li, X., Tang, Y., Li, H., Dong, B., and Zhi, C. (2020). Dendrites in Zn-based batteries. Adv. Mater. *32*, 2001854.
2. Dawut, G., Lu, Y., Miao, L., and Chen, J. (2018). High-performance rechargeable aqueous Zn-ion batteries with a poly(benzoquinonyl sulfide) cathode. Inorg. Chem. Front. *5*, 1391-1396.
3. Zhang, N., Cheng, F., Liu, J., Wang, L., Long, X., Liu, X., Li, F., and Chen, J. (2017). Rechargeable aqueous zinc-manganese dioxide batteries with high energy and power densities. Nat. Comm. *8*, 405.
4. Guo, Z., Ma, Y., Dong, X., Huang, J., Wang, Y., and Xia, Y. (2018). An environmentally friendly and flexible aqueous zinc battery using an organic cathode. Angew. Chem. Int. Ed. *57*, 11737-11741.
5. Xiong, T., Yu, Z.G., Wu, H., Du, Y., Xie, Q., Chen, J., Zhang, Y.-W., Pennycook, S.J., Lee, W.S.V., and Xue, J. (2019). Defect engineering of oxygen-deficient manganese oxide to achieve high-performing aqueous zinc ion battery. Adv. Energy Mater. *9*, 1803815.
6. Zhao, Q., Huang, W., Luo, Z., Liu, L., Lu, Y., Li, Y., Li, L., Hu, J., Ma, H., and Chen, J. (2018). High-capacity aqueous zinc batteries using sustainable quinone electrodes. Sci. Adv. *4*, 1761.
7. Jiao, T., Yang, Q., Wu, S., Wang, Z., Chen, D., Shen, D., Liu, B., Cheng, J., Li, H., Ma, L., et al. (2019). Binder-free hierarchical VS_2 electrodes for high-performance aqueous Zn ion batteries towards commercial level mass loading. J. Mater. Chem. A *7*, 16330-16338.
8. Song, Z., Qian, Y., Zhang, T., Otani, M., and Zhou, H. (2015). Poly(benzoquinonyl sulfide) as a high-energy organic cathode for rechargeable Li and Na batteries. Adv. Sci. *2*, 1500124.
9. Tang, F., Zhou, W., Chen, M., Chen, J., and Xu, J. (2019). Flexible free-standing paper electrodes based on reduced graphene oxide/δ-$Na_xV_2O_5{\cdot}nH_2O$ nanocomposite for high-performance aqueous zinc-ion batteries. Electrochim. Acta *328*, 135137.
10. Liu, P., Liu, W., Huang, Y., Li, P., Yan, J., and Liu, K. (2020). Mesoporous hollow carbon spheres boosted, integrated high performance aqueous Zn-Ion energy storage. Energy Storage Mater. *25*, 858-865.
11. Ma, H., Tian, X., Wang, T., Tang, K., Liu, Z., Hou, S., Jin, H., and Cao, G. (2021). Tailoring pore structures of 3D printed cellular high-loading cathodes for advanced rechargeable zinc-ion batteries. Small *17*, 2100746.
12. Leng, K., Li, G., Guo, J., Zhang, X., Wang, A., Liu, X., and Luo, J. (2020). A safe polyzwitterionic hydrogel electrolyte for long-life quasi-solid state zinc metal batteries. Adv. Funct. Mater. *30*, 2001317.
13. Shinde, S.S., Jung, J.Y., Wagh, N.K., Lee, C.H., Kim, D.-H., Kim, S.-H., Lee, S.U., and Lee, J.-H. (2021). Ampere-hour-scale zinc–air pouch cells. Nat. Energy *6*, 592-604.
14. Hou, Z., Tan, H., Gao, Y., Li, M., Lu, Z., and Zhang, B. (2020). Tailoring desolvation kinetics enables stable zinc metal anodes. J. Mater. Chem. A *8*, 19367-19374.
15. Chen, M., Chen, J., Zhou, W., Xu, J., and Wong, C.-P. (2019). High-performance flexible and self-healable quasi-solid-state zinc-ion hybrid supercapacitor based

on borax-crosslinked polyvinyl alcohol/nanocellulose hydrogel electrolyte. J. Mater. Chem. A *7*, 26524-26532.

16. Han, Q., Chi, X., Liu, Y., Wang, L., Du, Y., Ren, Y., and Liu, Y. (2019). An inorganic salt reinforced Zn^{2+}-conducting solid-state electrolyte for ultra-stable Zn metal batteries. J. Mater. Chem. A *7*, 22287-22295.
17. Zhu, M., Wang, X., Tang, H., Wang, J., Hao, Q., Liu, L., Li, Y., Zhang, K., and Schmidt, O.G. (2020). Antifreezing hydrogel with high zinc reversibility for flexible and durable aqueous batteries by cooperative hydrated cations. Adv. Funct. Mater. *30*, 1907218.
18. Naveed, A., Yang, H., Yang, J., Nuli, Y., and Wang, J. (2019). Highly reversible and rechargeable safe Zn batteries based on a triethyl phosphate electrolyte. Angew. Chem. Int. Ed. *58*, 2760-2764.
19. Ma, L., Chen, S., Li, N., Liu, Z., Tang, Z., Zapien, J.A., Chen, S., Fan, J., and Zhi, C. (2020). Hydrogen-free and dendrite-free all-solid-state Zn-ion batteries. Adv. Mater. *32*, 1908121.
20. Wang, N., Yang, Y., Qiu, X., Dong, X., Wang, Y., and Xia, Y. (2020). Stabilized rechargeable aqueous zinc batteries using ethylene glycol as water blocker. ChemSusChem *13*, 5556-5564.
21. Zhao, J., Zhang, J., Yang, W., Chen, B., Zhao, Z., Qiu, H., Dong, S., Zhou, X., Cui, G., and Chen, L. (2019). “Water-in-deep eutectic solvent” electrolytes enable zinc metal anodes for rechargeable aqueous batteries. Nano Energy *57*, 625-634.
22. Liang, P., Yi, J., Liu, X., Wu, K., Wang, Z., Cui, J., Liu, Y., Wang, Y., Xia, Y., and Zhang, J. (2020). Highly reversible Zn anode enabled by controllable formation of nucleation sites for Zn-based batteries. Adv. Funct. Mater. *30*, 1908528.
23. Chen, C.-Y., Matsumoto, K., Kubota, K., Hagiwara, R., and Xu, Q. (2019). A room-temperature molten hydrate electrolyte for rechargeable zinc–air batteries. Adv. Energy Mater. *9*, 1900196.
24. Wang, F., Borodin, O., Gao, T., Fan, X., Sun, W., Han, F., Faraone, A., Dura, J.A., Xu, K., and Wang, C. (2018). Highly reversible zinc metal anode for aqueous batteries. Nat. Mater. *17*, 543-549.
25. Yin, Y., Wang, S., Zhang, Q., Song, Y., Chang, N., Pan, Y., Zhang, H., and Li, X. (2020). Dendrite-free zinc deposition induced by Tin-modified multifunctional 3D host for stable zinc-based flow battery. Adv. Mater. *32*, 1906803.
26. Xu, W., Zhao, K., Huo, W., Wang, Y., Yao, G., Gu, X., Cheng, H., Mai, L., Hu, C., and Wang, X. (2019). Diethyl ether as self-healing electrolyte additive enabled long-life rechargeable aqueous zinc ion batteries. Nano Energy *62*, 275-281.